Available online at www.sciencedirect.com
ScienceDirect
Journal of Molecular Spectroscopy 242 (2007) 182–194
Journal of MOLECULAR SPECTROSCOPY
www.elsevier.com/locate/jms

Spin–orbit coupling of the NaK $3^3\Pi$ and $3^1\Pi$ states: Determination of the coupling constant and observation of quantum interference effects

S. Eckel [1], S. Ashman, J. Huennekens *

Department of Physics, 16 Memorial Drive East, Lehigh University, Bethlehem, PA 18015, USA

Received 8 December 2006; in revised form 3 February 2007
Available online 15 February 2007

Abstract

We have studied the mutually perturbing $3^3\Pi_{\Omega=0}(v=32, J=19) \sim 3^1\Pi_{\Omega=1}(v=6, J=19)$ levels of NaK that are coupled together by the spin–orbit interaction. We note that this coupling is nominally forbidden by the $\Delta\Omega = 0$ selection rule for spin–orbit perturbations. However $3^3\Pi$ levels labeled by different values of Ω are mixed by rotational coupling; i.e. the $3^3\Pi_\Omega$ levels are best described by a coupling scheme intermediate between Hund's cases (a) and (b). Thus the $3^1\Pi_{\Omega=1}$ level couples to the $3^3\Pi_{\Omega=0}$ level via the small admixture of $3^3\Pi_{\Omega=1}$ character in the latter. The $3^3\Pi_{\Omega=0}(v=32, J=19) \sim 3^1\Pi_{\Omega=1}(v=6, J=19)$ f symmetry pair is of particular interest since it appears to be very close to a 50–50 mixture of triplet and singlet character, and the splitting between these levels provides a direct measure of the $3^3\Pi \sim 3^1\Pi$ spin–orbit coupling constant. On the other hand, excitation spectra of the $3^3\Pi_{\Omega=0}(v=32, J=19) \sim 3^1\Pi_{\Omega=1}(v=6, J=19)$ e symmetry pair through the mixed "window" levels $1(b)^3\Pi_{\Omega=0}(v=17, J=18, 20) \sim 2(A)^1\Sigma^+(v=18,\ J=18, 20)$ display dramatic quantum interference effects associated with "singlet" and "triplet" excitation channels. Almost complete cancellation for populating one or the other of the two upper states is observed for excitation from the predominantly triplet members of the window level pairs.

Keywords: Diatomic molecules; NaK; Molecular spectroscopy; OODR; Spin-Orbit interaction; Quantum interference

1. Introduction

Alkali diatomic molecules have long been an active testing ground for theoretical quantum chemistry codes and are of current interest for cooling and trapping studies. Heteronuclear alkali molecules have permanent dipole moments and are, therefore, of particular interest because, in principle, they can be oriented in an optical lattice [1–7]. In our laboratory at Lehigh University we have carried out a series of high-resolution spectroscopic studies of various excited electronic states of the heteronuclear alkali diatomic molecule NaK [8–17]. We have been particularly interested in the fine and hyperfine structure of these states and how variations in these structures with vibrational and rotational quantum numbers reflect changes in the electronic wavefunction with internuclear separation.

Spin–orbit interactions coupling individual levels of singlet and triplet states result in levels of mixed singlet-triplet character. Such mixed levels are important since they can be used to gain access to higher alkali triplet states. The "perturbation-facilitated optical-optical double resonance" (PFOODR) technique, pioneered by Li and Field [18], is based upon pumping mixed singlet–triplet "window" levels (most often coupled levels of the $A^1\Sigma^+$ and $b^3\Pi_0$ states) from the singlet ground state and then probing from these window levels to higher triplets. PFOODR spectroscopy has been used to obtain detailed information on both homonuclear and heteronuclear alkali diatomic molecule triplet states including hyperfine structure [19–46]. The spin–orbit interactions themselves are also of interest since they provide an important mechanism for collisional exci-

* Corresponding author. Fax: +1 610 758 5730.
E-mail address: jph7@lehigh.edu (J. Huennekens).
[1] Present address: Sloane Physics Lab, 217 Prospect Street, Yale University, New Haven, CT 06511, USA.

0022-2852/$ - see front matter © 2007 Elsevier Inc. All rights reserved.
doi:10.1016/j.jms.2007.02.012

tation transfer between various atomic and molecular states.

Quantum interference effects are also of current interest and can be observed in atomic and molecular systems whenever there is more than one quantum mechanical pathway leading to the same final state [47–52]. Such interference effects form the basis of many interesting phenomena including most quantum control schemes [53–64].

In the present work, we investigate the spin–orbit interactions between the $3^1\Pi_{\Omega=1}(v=6)$ and $3^3\Pi_{\Omega=0,1,2}(v=32)$ levels of NaK. All three components of the $3^3\Pi$ state are perturbed by $3^1\Pi$ levels at different values of J, and the $3^3\Pi_{\Omega=0}(v=32,J=19) \sim 3^1\Pi_{\Omega=1}(v=6,J=19)$ f symmetry pair is an almost perfect 50–50 mixture of singlet and triplet character. We analyze these data to determine the $3^3\Pi(v=32)$ spin–orbit coupling constant and the $3^3\Pi_{\Omega=1}(v=32) \sim 3^1\Pi_{\Omega=1}(v=6)$ spin–orbit interaction parameter. We also observe dramatic quantum interference effects when we excite the $3^3\Pi_{\Omega=0}(v=32,J=19) \sim 3^1\Pi_{\Omega=1}(v=6,J=19)$ e symmetry pair from mixed $1(b)^3\Pi_{\Omega=0}(v=17,J=18,20) \sim 2(A)^1\Sigma^+(v=18,J=18,20)$ intermediate state window levels. Analysis of the constructive and destructive interference of the singlet and triplet channels allows us to determine the upper and intermediate state mixing amplitudes, the ratio of the singlet to triplet channel dipole matrix elements associated with this excitation step, and the ratio of the singlet to triplet radiative decay rates out of the upper states.

This paper is organized as follows. Section 2 describes the experimental setup. The data and analysis leading to the determination of the NaK $3^3\Pi \sim 3^1\Pi$ spin–orbit interaction parameter and other molecular constants are described in Section 3. Quantum interference effects in the excitation of the $3^3\Pi_{\Omega=0}(v=32,J=19,\ e) \sim 3^1\Pi_{\Omega=1}(v=6,J=19,\ e)$ levels is discussed in Section 4. Finally, a few concluding remarks can be found in Section 5.

2. The experiment

The optical–optical double resonance (OODR) experimental setup has been described in detail in Ref. [12] and is shown in Fig. 1 of that reference. A mixture of sodium and potassium metals is contained in a five-arm, stainless steel heat pipe oven that is heated to a temperature in the range 330–360 °C to produce a vapor of NaK molecules (in addition to atomic sodium and potassium and Na_2 and K_2 molecules). Argon gas, in the pressure range 0.9–2.5 Torr, is used as a buffer gas to keep the hot alkali vapor from reaching the oven windows.

We use a single-mode cw dye laser (the "pump" laser—Coherent model 699-29) to excite NaK molecules from a selected ro-vibrational level of the molecular ground state $1(X)^1\Sigma^+$ to the "intermediate state", which is a level of the $2(A)^1\Sigma^+$ electronic state or a level with mixed $1(b)^3\Pi_\Omega \sim 2(A)^1\Sigma^+$ character [8,9,12,14,15]. The mixed levels $1(b)^3\Pi_\Omega(v_b,J) \sim 2(A)^1\Sigma^+(v_A,J)$, often called window levels because they allow access into the triplet manifold of states, occur when nearly degenerate levels of the two electronic states, with the same rotational number J, are coupled together by the spin–orbit interaction. Once a particular intermediate state is located, the pump laser is adjusted to the transition frequency and fixed.

A single mode cw Ti:Sapphire laser (the "probe" laser—Coherent model 899-29) is used to further excite the molecules from the intermediate state to a level of the upper state, which can be either the $3^1\Pi_{\Omega=1}$ or the $3^3\Pi_{\Omega=0,1,2}$ state, or to a level with mixed $3^3\Pi_{\Omega=0,1,2} \sim 3^1\Pi_{\Omega=1}$ character. The upper levels radiate down to the $1(a)^3\Sigma^+$ state and/or the $1(X)^1\Sigma^+$ state. As the Ti:Sapphire laser is scanned over transitions to levels of the upper states, we monitor bound-free $3^3\Pi_\Omega \rightarrow 1(a)^3\Sigma^+$ fluorescence in the green part of the spectrum or bound-bound $3^1\Pi_1 \rightarrow 1(X)^1\Sigma^+$ fluorescence in the violet (excitation spectra) using a Hamamatsu R-928 photomultiplier tube (PMT) equipped with appropriate filters.

The dye laser is calibrated by comparing laser-induced fluorescence from an iodine cell with lines listed in the I_2 spectral atlas [65]. The Ti:Sapphire laser is calibrated using optogalvanic spectra from a hollow cathode lamp containing neon gas. We believe that upper state level energies are measured to within an absolute accuracy of $\sim 0.02\ cm^{-1}$. Relative energies, such as splittings between hyperfine components, can be measured with a much higher precision, which we estimate to be $0.001\ cm^{-1}$ (30 MHz).

3. NaK $3^3\Pi \sim 3^1\Pi$ spin–orbit coupling

Fig. 1b shows excitation spectra associated with the NaK $3^3\Pi_0(v=32,J=19,\ f) \sim 3^1\Pi_1(v=6,J=19,\ f) \leftarrow 2(A)^1\Sigma^+(v=16,\ J=19) \leftarrow 1(X)^1\Sigma^+(v=0,J=20)$ OODR transitions. Levels of the upper Π states ($\Lambda=1$) are doubly degenerate due to lambda doubling. The e and f symmetry components are typically separated from each other by energies on the order of 10^{-3}–$10^{-2}\ cm^{-1}$ or less, due to small interactions with remote states. All levels of the $^1\Sigma^+$ states have e symmetry, and for the data shown in Fig. 1b we only access f symmetry levels of the upper states due to the selection rule $e \leftrightarrow f$ only for $\Delta J=0$ transitions, while $e \leftrightarrow e$, $f \leftrightarrow f$, but $e \not\leftrightarrow f$ for $\Delta J=\pm 1$ transitions.

Because of the $\Delta S=0$ dipole selection rule and the fact that the intermediate state $2(A)^1\Sigma^+(v=16,J=19)$ is a fairly pure (i.e. relatively unperturbed) singlet level, we know that the upper levels must possess substantial singlet character. On the other hand, the dominant hyperfine interaction in all alkali molecules is the Fermi contact interaction $b_F\mathbf{I}\cdot\mathbf{S}$. And because both upper levels display appreciable hyperfine structure and broadening we therefore know that both upper levels must also possess significant triplet character (i.e. have some amplitude corresponding to $S \neq 0$).

In fact, the spectrum shown in Fig. 1b displays two mirror image lines of nearly equal intensity and almost exactly the same hyperfine splittings. We therefore conclude that

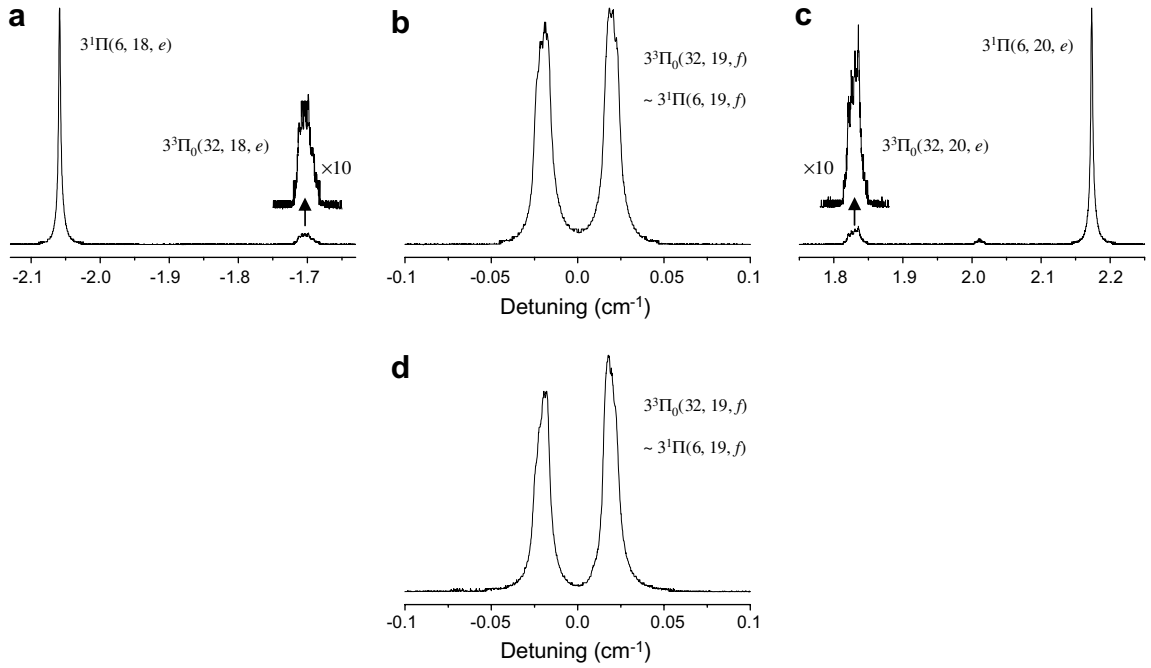

Fig. 1. NaK PFOODR excitation lines recorded as the probe laser frequency is scanned while total bound-free $3^3\Pi_0 \rightarrow 1(a)^3\Sigma^+$ (green) or bound-bound $3^1\Pi \rightarrow 1(X)^1\Sigma^+$ (violet) fluorescence is monitored. (a) $3^3\Pi_0(v = 32, J = 18, e) \sim 3^1\Pi(v = 6, J = 18, e) \leftarrow 2(A)^1\Sigma^+(v = 16, J = 19)$ transitions (with green fluorescence detection); (b) $3^3\Pi_0(v = 32, J = 19, f) \sim 3^1\Pi(v = 6, J = 19, f) \leftarrow 2(A)^1\Sigma^+(v = 16, J = 19)$ transitions (green); (c) $3^3\Pi_0(v = 32, J = 20, e) \sim 3^1\Pi(v = 6, J = 20, e) \leftarrow 2(A)^1\Sigma^+(v = 16, J = 19)$ transitions (green); and (d) $3^3\Pi_0(v = 32, J = 19, f) \sim 3^1\Pi(v = 6, J = 19, f) \leftarrow 2(A)^1\Sigma^+(v = 16, J = 19)$ transitions (violet).

each of these two upper levels is an almost perfect 50–50 singlet/triplet mixture. (Later we will present evidence verifying this conjecture.) We carried out calculations based on the published molecular constants of the NaK $3^1\Pi$ state [11,66] and the reported levels of the NaK $3^3\Pi$ state (EPAPS Table 2 of Ref. 15) which indicate that the unperturbed $3^1\Pi_1(v = 6, J = 19)$ and $3^3\Pi_0(v = 32, J = 19)$ levels should indeed be nearly degenerate and lie at the appropriate energy necessary to identify them with the levels observed in the figure.

Figs. 1a and c show the $3^3\Pi_0(v = 32, J = 18, e) \sim 3^1\Pi_1(v = 6, J = 18, e) \leftarrow 2(A)^1\Sigma^+(v = 16, J = 19)$ and $3^3\Pi_0(v = 32, J = 20, e) \sim 3^1\Pi_1(v = 6, J = 20, e) \leftarrow 2(A)^1\Sigma^+(v = 16, J = 19)$ excitation spectra. Here we populate upper state levels of e symmetry since the probe transitions involve $\Delta J = \pm 1$. Again we note that from an intermediate singlet level it is only possible to observe upper levels possessing some singlet character. The levels with predominant triplet character are weak in these scans because the mixing here is much less than in the $J = 19$ pair, due to the fact that the mutually perturbing $J = 18$ and $J = 20$ levels are much further separated in energy than the $J = 19$ levels.

Spin–orbit coupling between levels of the $3^1\Pi_{\Omega=1}$ state and levels of the $3^3\Pi_{\Omega=0}$ or $3^3\Pi_{\Omega=2}$ state with the same J value is nominally forbidden by the $\Delta\Omega = 0$ selection rule for spin–orbit perturbations. However $3^3\Pi$ levels labeled by different values of Ω are mixed by rotational coupling; i.e., the $3^3\Pi_\Omega$ levels are best described by a coupling scheme intermediate between Hund's cases (a) and (b). Thus a $3^1\Pi_{\Omega=1}$ level can couple to $3^3\Pi_{\Omega=0,2}$ levels via the small admixture of $3^3\Pi_{\Omega=1}$ character in the latter.

Because both members of the $3^3\Pi_0(v = 32, J = 19, f) \sim 3^1\Pi_1(v = 6, J = 19, f)$ level pair appear to be almost perfect 50–50 singlet/triplet mixtures, it can be assumed that the corresponding unperturbed levels (i.e., those that would be observed if the spin–orbit coupling could be turned off) must be almost exactly degenerate. In such a case, it is straightforward to diagonalize the 2×2 Hamiltonian matrix and show that the perturbed (measured) levels will be separated in energy by

$$\Delta E = 2|\langle 3^3\Pi_0(v = 32, J = 19, e)|H_{SO}|3^1\Pi(v = 6, J = 19, e)\rangle| \equiv 2|H_{SO}|. \quad (1)$$

In the present case we find $\Delta E = 0.0397\ \text{cm}^{-1}$ and therefore $|H_{SO}| = 0.0199\ \text{cm}^{-1}$. If we write the wavefunction of each $3^3\Pi$ level using a Hund's case (a) basis:

$$|\Psi\rangle = a_0|3^3\Pi_{\Omega=0}\rangle + a_1|3^3\Pi_{\Omega=1}\rangle + a_2|3^3\Pi_{\Omega=2}\rangle, \quad (2)$$

we can relate the $3^3\Pi_{\Omega=1}(v = 32) \sim 3^1\Pi_{\Omega=1}(v = 6)$ spin–orbit interaction constant ξ to the measured $|H_{SO}|$ value by the $3^3\Pi_{\Omega=1}$ amplitude, a_1, in the level that we nominally identify as $3^3\Pi_{\Omega=0}(v = 32, J = 19, f)$, i.e.,

$$|\xi| = \frac{|H_{SO}|}{|a_1|}. \quad (3)$$

Energies of a number of $3^1\Pi_{\Omega=1}(v = 6, J)$ and $3^3\Pi_{\Omega=0,1,2}(v = 32, J)$ levels were measured using

several pure singlet intermediate states $2(A)^1\Sigma^+(v_A, J')$ and several mixed singlet/triplet intermediate states $1(b)^3\Pi_{\Omega=0,1,2}(v_b, J') \sim 2(A)^1\Sigma^+(v_A, J')$. These $3^1\Pi_1(v=6, J)$ and $3^3\Pi_{0,1,2}(v=32, J)$ level energies are listed in a table, which is available electronically in the JMS Supplementary materials [67], along with pump and probe laser frequencies and energies of the ground state level involved in each OODR transition.

We carried out a full deperturbation of the $3^3\Pi_{\Omega=0,1,2}(v=32) \sim 3^1\Pi_{\Omega=1}(v=6)$ system using the deperturbation program LSQ [68]. The full $3^3\Pi_{\Omega=0,1,2}(v=32) \sim 3^1\Pi_{\Omega=1}(v=6)$ Hamiltonian matrix can be written in the following form:

$$
\begin{array}{c}
 \\
3^1\Pi_{\Omega=1} \\
3^3\Pi_{\Omega=0} \\
3^3\Pi_{\Omega=1} \\
3^3\Pi_{\Omega=2}
\end{array}
\begin{array}{c}
\begin{array}{cccc}
3^1\Pi_{\Omega=1} & 3^3\Pi_{\Omega=0} & 3^3\Pi_{\Omega=1} & 3^3\Pi_{\Omega=2}
\end{array} \\
\begin{pmatrix}
T_{v_S=6} + B_{v_S=6}[x-1] \\ -D_{v_S=6}(x-1)^2 \\ +q_{v_S=6}\lambda(x-1)
& 0 & \xi & 0 \\
0 & \begin{array}{l} T_{v_T=32} - A_{v_T=32} + B_{v_T=32}(x+1) \\ -D_{v_T=32}(x^2+4x+1) \\ +H_{v_T=32}(x^3+9x^2+9x+1) \end{array} & \begin{array}{l} \sqrt{2x}\{-B_{v_T=32} + 2D_{v_T=32}(x+1) \\ +H_{v_T=32}(3x^2+10x-1)\} \end{array} & \begin{array}{l} -2\sqrt{x(x-2)}\{-D_{v_T=32} \\ +H_{v_T=32}(3x-1)\} \end{array} \\
\xi & \begin{array}{l} \sqrt{2x}\{-B_{v_T=32} + 2D_{v_T=32}(x+1) \\ +H_{v_T=32}(3x^2+10x-1)\} \end{array} & \begin{array}{l} T_{v_T=32} + B_{v_T=32}(x+1) \\ -D_{v_T=32}(x^2+6x-3) \\ +H_{v_T=32}(x^3+15x^2-5x+5) \end{array} & \begin{array}{l} \sqrt{2(x-2)}\{-B_{v_T=32} \\ +2D_{v_T=32}(x-1) \\ +H_{v_T=32}(3x^2-2x+3)\} \end{array} \\
0 & \begin{array}{l} -2\sqrt{x(x-2)}\{-D_{v_T=32} \\ +H_{v_T=32}(3x-1)\} \end{array} & \begin{array}{l} \sqrt{2(x-2)}\{-B_{v_T=32} \\ +2D_{v_T=32}(x-1) \\ +H_{v_T=32}(3x^2-2x+3)\} \end{array} & \begin{array}{l} T_{v_T=32} + A_{v_T=32} + B_{v_T=32}(x-3) \\ -D_{v_T=32}(x^2-4x+5) \\ +H_{v_T=32}(x^3-3x^2+5x-7) \end{array}
\end{pmatrix}
\end{array}. \quad (4)
$$

Here the subscripts S and T stand for singlet and triplet and $x \equiv J(J+1)$. In addition, T_v is the band origin (electronic plus vibrational energy), B_v is the rotational constant, and D_v and H_v are the centrifugal distortion constants for each state. A_v is the $3^3\Pi$ state spin–orbit constant, ξ is the $3^3\Pi \sim 3^1\Pi$ spin–orbit coupling constant and q_v is the $3^1\Pi$ Λ-doubling constant. λ is a parameter that is equal to 0 for f parity levels and 1 for e parity levels. Other small terms, including Λ-doubling (o, p, q parameters) for the $3^3\Pi$ state, hyperfine structure, spin-rotation coupling, and spin-spin interactions, are neglected.

The deperturbation program allows some parameters to be fixed, while others are varied. Initial values of the fitted parameters are chosen and the matrix is diagonalized separately for each value of J. Calculated level energies are then compared to the measured energies and the parameters are varied until the calculated and measured energies agree in the least squares sense. In our present work we fixed the spectroscopic constants T_v, B_v, D_v, and q_v of the $3^1\Pi(v=6)$ state to the values reported in the erratum to Laub et al. [11] (but corrected for the slight difference between the ground state constants of Ross et al. [69] and the more accurate, recent values of Russier et al. [70]). In general, the $3^1\Pi$ state constants of Pashov et al. [66] are probably superior to those of Laub et al., but the latter were chosen for the present work because they cover the same range of vibrational and rotational levels as those investigated here and are also based upon the same calibration. In the first step of the fitting procedure, the $3^3\Pi \sim 3^1\Pi$ spin–orbit coupling parameter ξ was fixed at zero and the spectroscopic constants T_v, A_v, B_v, D_v, and H_v of the $3^3\Pi(v=32)$ state were varied to give the best fit of the $3^3\Pi$ level energies. The fitting program output provides the squares of the $3^3\Pi$ rotational mixing amplitudes a_0, a_1, and a_2 [see Eq. (2)]. We used the value of a_1 (0.3476) for the level with predominant $3^3\Pi_{\Omega=0}(v=32, J=19, f)$ character and the value of $|H_{SO}|$ obtained from the $3^3\Pi_0(v=32, J=19,\ f) \sim 3^1\Pi_1(v=6, J=19,\ f)$ data as described above in Eq. (3) to determine the magnitude of the coupling parameter

Table 1
Molecular constants describing the NaK $3^1\Pi_{\Omega=1}(v=6,J)$ and $3^3\Pi_{\Omega=0,1,2}(v=32,J)$ rotational levels and their spin–orbit coupling

$3^1\Pi_{\Omega=1}(v=6,J)$ constants and the $3^3\Pi_{\Omega=1}(v=32)\sim 3^1\Pi_{\Omega=1}(v=6)$ spin–orbit interaction constant (not varied in fit)	$3^3\Pi_{\Omega=0,1,2}(v=32,J)$ constants (varied in fit)
$T_{v_S=6} = 25820.411\ \text{cm}^{-1}$	$T_{v_T=32} = (25826.868 \pm 0.003)\ \text{cm}^{-1}$
$B_{v_S=6} = 0.054458\ \text{cm}^{-1}$	$B_{v_T=32} = (0.047401 \pm 0.000016)\ \text{cm}^{-1}$
$D_{v_S=6} = 3.295 \times 10^{-7}\ \text{cm}^{-1}$	$D_{v_T=32} = (1.8432 \pm 0.0135) \times 10^{-6}\ \text{cm}^{-1}$
$q_{v_S=6} = 2.0 \times 10^{-5}\ \text{cm}^{-1}$	$H_{v_T=32} = (1.4949 \pm 0.0159) \times 10^{-10}\ \text{cm}^{-1}$
$\lvert\xi\rvert = (0.0572 \pm 0.0013)\ \text{cm}^{-1}$	$A_{v_T=32} = (3.179 \pm 0.005)\ \text{cm}^{-1}$

$3^1\Pi_{\Omega=1}(v=6)$ constants were fixed at the values given in Ref. [11] (corrected using the recent ground state constants of Russier et al. [70]). The $3^3\Pi_{\Omega=1}(v=32)\sim 3^1\Pi_{\Omega=1}(v=6)$ spin–orbit interaction constant $|\xi|$ was obtained from the average splitting of the mutually perturbing $3^3\Pi_{\Omega=0}(v=32,J=19,f)\sim 3^1\Pi_{\Omega=1}(v=6,J=19,f)$ levels, as described in the text. Uncertainties listed in the table represent statistical error bars only (1σ).

$$|\xi| = (0.0572 \pm 0.0014)\ \text{cm}^{-1}, \tag{5}$$

where the error bar is statistical (1σ). We believe that this value of $|\xi|$ is more accurate than the value that is obtained by allowing this parameter to vary in the deperturbation analysis [$|\xi| = (0.054 \pm 0.013)\text{cm}^{-1}$]. Next we carried out a second round of deperturbation by setting $\xi = 0.0572\ \text{cm}^{-1}$ and refitting the parameters T_v, A_v, B_v, D_v, and H_v for the $3^3\Pi(v=32)$ state. Final values of all the best fit parameters are provided in Table 1. A plot of the measured and calculated energies is shown in Fig. 2.

As described in Refs. [9,14], and [52] the magnitude of the spin–orbit matrix element ξ is given approximately as a product of an electronic term $|H_{\text{el}}|$ times a vibrational overlap integral:

$$|\xi| = |H_{\text{el}}| \cdot |\langle 3^3\Pi(v_T=32)|3^1\Pi(v_S=6)\rangle|. \tag{6}$$

We calculated the vibrational overlap integral to be $|\langle 3^3\Pi(v_T=32)\ |3^1\Pi(v_S=6)\rangle| = 0.0174$ using Le Roy's program LEVEL [71], and the $3^3\Pi$ and $3^1\Pi$ potentials from Refs. [15] and [11], respectively. From this, we found

$$|H_{\text{el}}| = (3.29 \pm 0.07)\ \text{cm}^{-1}. \tag{7}$$

For isoconfigurational $^1\Pi$ and $^3\Pi$ states, $|H_{\text{el}}|$ should be compared to the essentially identical value of the $3^3\Pi$ state spin–orbit constant $A_{v_T=32}$. In the present work, we obtained the value $A_{v_T=32} = (3.179 \pm 0.005)\ \text{cm}^{-1}$, which is consistent with $|H_{\text{el}}|$ and with A_{v_T} values obtained for many different NaK $3^3\Pi$ vibrational levels that were reported in Ref. [15].

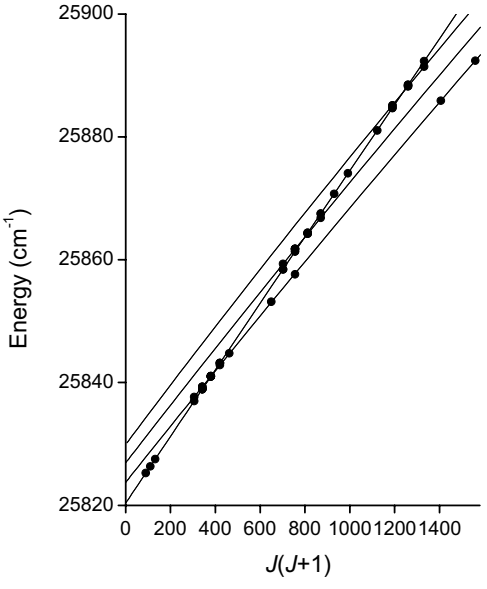

Fig. 2. Measured energies (solid circles) and calculated energies (solid lines) of the NaK $3^1\Pi_{\Omega=1}(v=6,J,\ e/f)$ and $3^3\Pi_{\Omega=0,1,2}(v=32,J,\ e/f)$ rovibrational levels plotted as a function of $J(J+1)$. The three parallel lines represent levels of the $3^3\Pi$ state $\Omega=0$, 1, and 2 components (from lowest to highest energy, respectively), while the line crossing diagonally from lower left to upper right represents $3^1\Pi$ levels. Energy splittings due to lambda doubling are too small to be seen in this diagram.

4. Quantum interference

It is well known that when more than one quantum mechanical path leads to the same final state, quantum interference effects may be observed (see Ref. [52], chapter 6 and references therein). Quantum interference effects are vividly displayed in the data presented in Fig. 3, which shows excitation spectra for the $3^3\Pi_{\Omega=0}(v=32, J=19)\sim 3^1\Pi_{\Omega=1}(v=6,J=19)$ e symmetry pair. In Fig. 3a, the $3^3\Pi_0(v=32,J=19,\ e)\sim 3^1\Pi_1(v=6,J=19,\ e)$ levels are excited from a "pure" singlet intermediate state $2(A)^1\Sigma^+(v=16,J=18)$, and no interference effects are observed. Each member of the pair of upper levels is a strong mixture of singlet and triplet amplitudes. However, as can be seen from the hyperfine structure displayed in Fig. 3a, the higher energy level clearly has slightly more triplet character while the lower energy level has slightly more singlet character. Figs. 3b and c show the same two upper levels excited through the predominantly triplet components of the mixed window levels $1(b)^3\Pi_0(v=17, J=18)\sim 2(A)^1\Sigma^+(v=18,J=18)$ and $1(b)^3\Pi_0(v=17, J=20)\sim 2(A)^1\Sigma^+(v=18,J=20)$, respectively. In each of these two cases, each upper state can be excited through two different quantum mechanical paths; a "singlet path" $3^1\Pi_1(v=6,J=19,\ e)\leftarrow 2(A)^1\Sigma^+(v=18,\ J'=J\pm 1)$ and a "triplet path" $3^3\Pi_0(v=32,J=19,\ e)\leftarrow 1(b)^3\Pi_0(v=17, J'=J\pm 1)$. As can be seen, almost complete destructive interference between the two excitation channels occurs for one or the other of the two upper states, depending on whether $J'=J-1$ or $J'=J+1$.

We can understand these observations by considering the following argument based upon the schematic energy

level diagram of Fig. 4. In the two-state approximation, the state function for each level of the upper $3^3\Pi_0(v=32, J=19, e) \sim 3^1\Pi_1(v=6, J=19, e)$ pair of levels (labeled $|3a\rangle$ and $|3b\rangle$ in Fig. 4) can be written as a linear combination of triplet and singlet amplitudes described by a mixing angle φ:

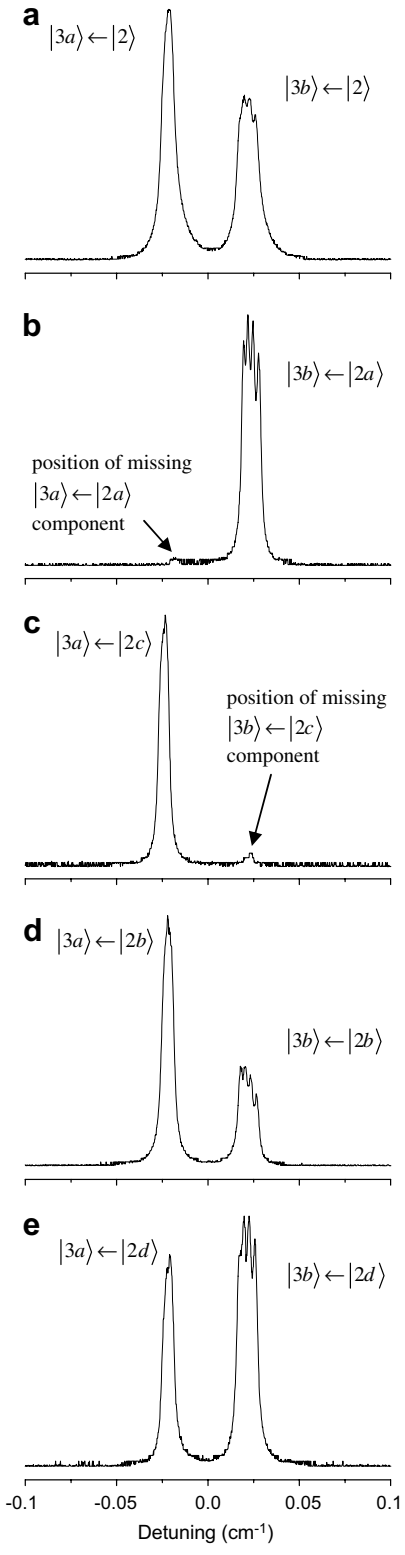

$$|3a\rangle = -\sin\varphi|3^3\Pi_0(v=32,J=19,e)\rangle + \cos\varphi|3^1\Pi_1(v=6,J=19,e)\rangle \quad (8a)$$

$$|3b\rangle = \cos\varphi|3^3\Pi_0(v=32,J=19,e)\rangle + \sin\varphi|3^1\Pi_1(v=6,J=19,e)\rangle. \quad (8b)$$

Here we note that it is always possible to choose a self-consistent set of phases such that all off-diagonal matrix elements of the Hamiltonian, transition moments, and mixing coefficients are real numbers [52,72,73]. It is straightforward to show that if the unperturbed triplet level lies higher in energy than the unperturbed singlet level, then

$$\cos\varphi = \frac{1}{\sqrt{2}}\left[1 + \frac{\Delta E^0/2}{[H_{SO}^2 + (\Delta E^0/2)^2]^{1/2}}\right]^{1/2} \geqslant 0, \quad (9a)$$

where $\Delta E^0 \equiv E_{3^3\Pi_0(v=32,J=19,e)} - E_{3^1\Pi(v=6,J=19,e)}$ is the energy difference between the unperturbed triplet and singlet levels, and $H_{SO} = \langle 3^3\Pi_0(v=32,J=19,\ e)|H_{SO}|3^1\Pi(v=6,\ J=19,\ e)\rangle$. Similarly,

$$\sin\varphi = \pm\frac{1}{\sqrt{2}}\left[1 - \frac{\Delta E^0/2}{[H_{SO}^2 + (\Delta E^0/2)^2]^{1/2}}\right]^{1/2} \quad (9b)$$

carries the same sign as H_{SO} [i.e. the upper sign in Eq. (9b) is used if $H_{SO} > 0$ and the lower sign is used if $H_{SO} < 0$]. If we now consider relatively weak excitation (so that stimulated emission terms can be neglected) to each of these levels from an intermediate state $|2\rangle$ that is a fairly pure singlet level such as $|2(A)^1\Sigma^+(v=16,\ J=18,\ e)\rangle$ (i.e., the dashed horizontal line and vertical arrows in Fig. 4), then we can write a steady-state rate equation for the population (n_{3i}) in either upper state ($i = a$ or b):

$$\dot{n}_{3i} = 0 = B_{3i\leftarrow 2} I_{probe} n_2 - \Gamma_{3i} n_{3i}, \quad (10)$$

with solution

$$n_{3i} = \frac{B_{3i\leftarrow 2} I_{probe} n_2}{\Gamma_{3i}}. \quad (11)$$

In these expressions, n_2 is the population in the intermediate level 2, Γ_{3i} is the total (radiative plus collisional) decay rate out of level $3i$, I_{probe} is the probe laser intensity, and $B_{3i\leftarrow 2}$ is the Einstein B coefficient for absorption to level $3i$ from level 2. Due to the selection rule on spin, $\Delta S = 0$, the Einstein B coefficient depends on the singlet channel dipole

Fig. 3. NaK PFOODR excitation lines demonstrating quantum interference effects. The probe laser frequency is scanned over transitions to the mixed $3^3\Pi(v=32, J=19,\ e) \sim 3^1\Pi(v=6, J=19,\ e)$ levels (levels $3a$ and $3b$ in Fig. 4) from various intermediate levels while total bound-free $3^3\Pi \rightarrow 1(a)^3\Sigma^+$ (green) fluorescence is monitored. The intermediate levels are (a) $2(A)^1\Sigma^+(v=16, J=18)$ (level 2); (b) the predominantly triplet component of the mixed pair $1(b)^3\Pi_0(v=17,\ J=18) \sim 2(A)^1\Sigma^+(v=18, J=18)$ (level $2a$); (c) the predominantly triplet component of the mixed pair $1(b)^3\Pi_0(v=17, J=20) \sim 2(A)^1\Sigma^+(v=18, J=20)$ (level $2c$); (d) the predominantly singlet component of the mixed pair $1(b)^3\Pi_0(v=17, J=18) \sim 2(A)^1\Sigma^+(v=18, J=18)$ (level $2b$); and (e) the predominantly singlet component of the mixed pair $1(b)^3\Pi_0(v=17,\ J=20) \sim 2(A)^1\Sigma^+(v=18, J=20)$ (level $2d$).

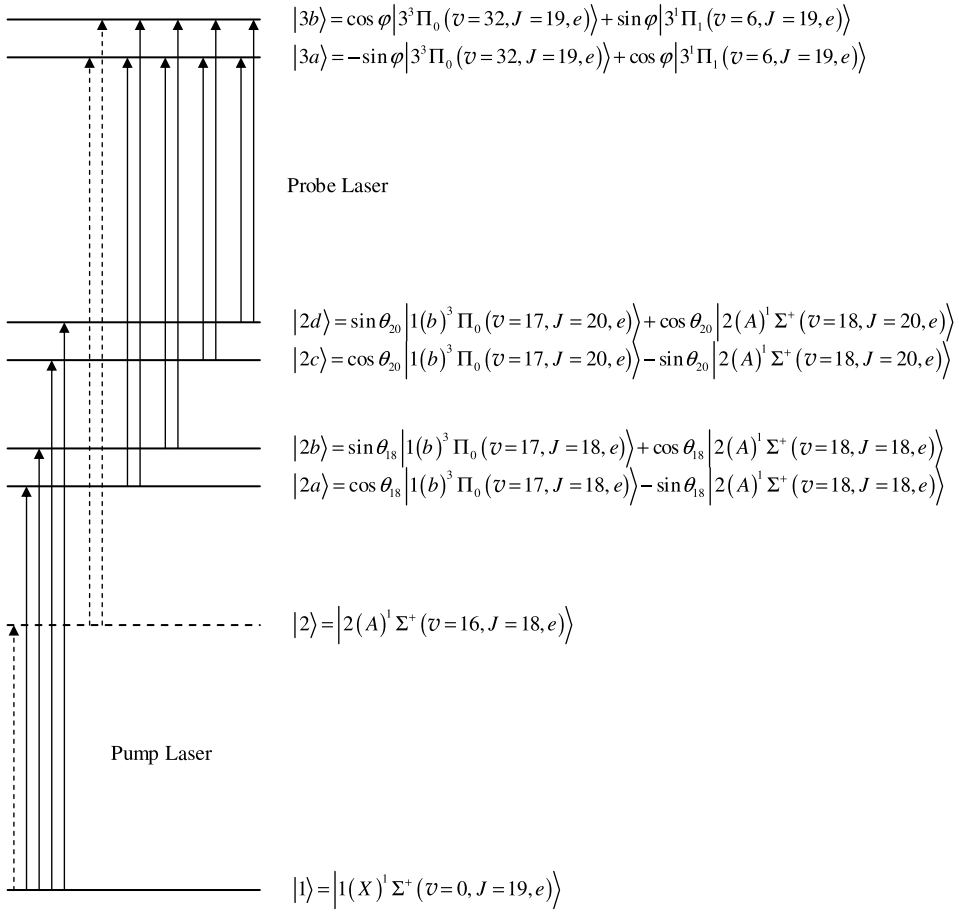

Fig. 4. Schematic energy level diagram showing the pump and probe laser transitions used to demonstrate quantum interference effects. The dashed arrows show excitation of the upper mixed $3^3\Pi(v=32,J=19,e) \sim 3^1\Pi(v=6,J=19,e)$ levels (levels 3*a* and 3*b*) through a "pure" singlet intermediate level $2(A)^1\Sigma^+(v=16,J=18)$ (level 2). The solid arrows show excitation of the same upper levels through the mixed intermediate levels $1(b)^3\Pi_0(v=17, J=18) \sim 2(A)^1\Sigma^+(v=18,J=18)$ and $1(b)^3\Pi_0(v=17,J=20) \sim 2(A)^1\Sigma^+(v=18,J=20)$ (levels 2*a*–2*d*).

matrix element squared, $|\langle 3^1\Pi_1(6,19)|\hat{\varepsilon}\cdot\vec{\mu}\,|A^1\Sigma^+(16,18)\rangle|^2$ ($\hat{\varepsilon}$ is the probe laser polarization vector), times the square of the singlet amplitude in the upper state ($\cos^2\varphi$ for state 3*a* and $\sin^2\varphi$ for state 3*b*).

For the data shown in Fig. 3, the excitation was monitored by detecting fluorescence in the green spectral range, corresponding to transitions from the upper state to the repulsive $1(a)^3\Sigma^+$ state. The fluorescence signal for level 3*i* is proportional to the upper state population n_{3i} times the radiative decay rate $\Gamma_{3i\to a^3\Sigma^+}$. Due to the dipole selection rule on spin, this radiative rate is equal to the triplet channel radiative rate $\Gamma_{3^3\Pi_0(32,19,e)\to a^3\Sigma^+}$ times the square of the upper state triplet amplitude. Thus using Eq. (11) and the relationship between the Einstein *B* coefficient and the dipole matrix element, we can write

$$\begin{aligned}(I_{3a\leftarrow 2})_{\text{green}} &\propto \varepsilon_{3^3\Pi\to a^3\Sigma^+}\sin^2\varphi\,\Gamma_{3^3\Pi\to a^3\Sigma^+}n_{3a}\\ &\propto \varepsilon_{3^3\Pi\to a^3\Sigma^+}\sin^2\varphi\frac{\Gamma_{3^3\Pi\to a^3\Sigma^+}}{\Gamma_{3a}}B_{3a\leftarrow 2}I_{\text{probe}}n_2\\ &\propto \varepsilon_{3^3\Pi\to a^3\Sigma^+}\sin^2\varphi\cos^2\varphi\frac{\Gamma_{3^3\Pi\to a^3\Sigma^+}}{\Gamma_{3a}}I_{\text{probe}}n_2\\ &\times|\langle 3^1\Pi_1(6,19)|\hat{\varepsilon}\cdot\vec{\mu}\,|A^1\Sigma^+(16,18)\rangle|^2,\end{aligned} \tag{12a}$$

and similarly

$$\begin{aligned}(I_{3b\leftarrow 2})_{\text{green}} &\propto \varepsilon_{3^3\Pi\to a^3\Sigma^+}\cos^2\varphi\,\Gamma_{3^3\Pi\to a^3\Sigma^+}n_{3b}\\ &\propto \varepsilon_{3^3\Pi\to a^3\Sigma^+}\cos^2\varphi\frac{\Gamma_{3^3\Pi\to a^3\Sigma^+}}{\Gamma_{3b}}B_{3b\leftarrow 2}I_{\text{probe}}n_2\\ &\propto \varepsilon_{3^3\Pi\to a^3\Sigma^+}\cos^2\varphi\sin^2\varphi\frac{\Gamma_{3^3\Pi\to a^3\Sigma^+}}{\Gamma_{3b}}I_{\text{probe}}n_2\\ &\times|\langle 3^1\Pi_1(6,19)|\hat{\varepsilon}\cdot\vec{\mu}\,|A^1\Sigma^+(16,18)\rangle|^2.\end{aligned} \tag{12b}$$

In these expressions, the subscripts "green" and $3i\leftarrow 2$ remind us that these are intensities of green fluorescence associated with transitions to the $1(a)^3\Sigma^+$ state measured when the upper state 3*i* is populated from the singlet level 2. Also, the factor $\varepsilon_{3^3\Pi\to a^3\Sigma^+}$ represents the average absolute detection system efficiency over the full range of $3^3\Pi_0(32,19,e)$ fluorescence wavelengths, the fluorescence collection solid angle divided by 4π, etc. Since the proportionality factor is the same in (12a) and (12b), we find that the intensity ratio for green fluorescence detection is given by

$$\left(\frac{I_{3a\leftarrow 2}}{I_{3b\leftarrow 2}}\right)_{\text{green}} = \frac{\Gamma_{3b}}{\Gamma_{3a}} = \left[\frac{\Gamma_{3^1\Pi_1(6,19,e)}\sin^2\varphi + \Gamma_{3^3\Pi_0(32,19,e)}\cos^2\varphi}{\Gamma_{3^1\Pi_1(6,19,e)}\cos^2\varphi + \Gamma_{3^3\Pi_0(32,19,e)}\sin^2\varphi}\right], \tag{13}$$

where in the last step we have written the total decay rate out of level $3i$ as a weighted sum of $3^1\Pi_1(6,19,e)$ and $3^3\Pi_0(32,19,e)$ decay rates.

If we carry out the same analysis for the situation where we only detect violet fluorescence, corresponding to radiative transitions terminating on the ground state $1(X)^1\Sigma^+$, we obtain

$$\left(\frac{I_{3a\leftarrow 2}}{I_{3b\leftarrow 2}}\right)_{\text{violet}} = \frac{\cos^4\varphi}{\sin^4\varphi}\frac{\Gamma_{3b}}{\Gamma_{3a}} = \frac{\cos^4\varphi}{\sin^4\varphi}\left[\frac{\Gamma_{3^1\Pi_1(6,19,e)}\sin^2\varphi + \Gamma_{3^3\Pi_0(32,19,e)}\cos^2\varphi}{\Gamma_{3^1\Pi_1(6,19,e)}\cos^2\varphi + \Gamma_{3^3\Pi_0(32,19,e)}\sin^2\varphi}\right]. \tag{14}$$

In this case, the factors $\sin^2\varphi\Gamma_{3^3\Pi\rightarrow a^3\Sigma^+}$ appearing in Eq. (12a) and $\cos^2\varphi\Gamma_{3^3\Pi\rightarrow a^3\Sigma^+}$ in Eq. (12b) for the green (triplet) fluorescence channel are replaced by $\cos^2\varphi\Gamma_{3^1\Pi\rightarrow X^1\Sigma^+}$ and $\sin^2\varphi\Gamma_{3^1\Pi\rightarrow X^1\Sigma^+}$ respectively in the violet (singlet) fluorescence channel. Thus when the ratio is taken, analogously to Eq. (13), the factor $\cos^2\varphi/\sin^2\varphi$ multiplies the $\cos^2\varphi/\sin^2\varphi$ from the excitation step to yield the $\cos^4\varphi/\sin^4\varphi$ appearing in Eq. (14). The upper state mixing angle is easily obtained from the ratio of these ratios:

$$\tan\varphi = \frac{\sin\varphi}{\cos\varphi} = \left[\frac{(I_{3a\leftarrow 2}/I_{3b\leftarrow 2})_{\text{green}}}{(I_{3a\leftarrow 2}/I_{3b\leftarrow 2})_{\text{violet}}}\right]^{1/4}. \tag{15}$$

From the measured ratios $(I_{3a\leftarrow 2}/I_{3b\leftarrow 2})_{\text{green}} = (1.06\pm 0.02)$ (Fig. 3a) and $(I_{3a\leftarrow 2}/I_{3b\leftarrow 2})_{\text{violet}} = (2.86\pm 0.16)$ (from similar data recorded with violet fluorescence filters) we obtain a preliminary value $|\varphi| = (38.0\pm 0.5)^\circ$ for the $3^3\Pi_0(v=32,J=19,\ e)\sim 3^1\Pi_1(v=6,J=19,\ e)$ mixing angle. However, since only $\tan^4\varphi$ is determined from the ratio of the green and violet fluorescence ratios, we cannot use these data to determine the sign of φ.

Finally, we can solve Eq. (13) for the ratio of the total decay rates out of the (unperturbed) $3^3\Pi_0(32,19,e)$ and $3^1\Pi_1(6,19,e)$ levels:

$$\frac{\Gamma_{3^3\Pi_0(32,19,e)}}{\Gamma_{3^1\Pi_1(6,19,e)}} = \frac{(\Gamma_{3b}/\Gamma_{3a}) - \tan^2\varphi}{1-(\Gamma_{3b}/\Gamma_{3a})\tan^2\varphi}. \tag{16}$$

The preliminary value $(\Gamma_{3b}/\Gamma_{3a}) \approx (I_{3a\leftarrow 2}/I_{3b\leftarrow 2})_{\text{green}} = (1.06\pm 0.02)$ yields $\Gamma_{3^3\Pi_0(32,19,e)}/\Gamma_{3^1\Pi_1(6,19,e)} \approx (1.27\pm 0.12)$. We note that these values for φ, Γ_{3b}/Γ_{3a}, and $\Gamma_{3^3\Pi_0(32,19,e)}/\Gamma_{3^1\Pi_1(6,19,e)}$ will be improved by a fitting procedure described below.

Next we consider excitation of levels $3a$ and $3b$ from one of the $J=18$ or $J=20$ mixed intermediate window levels $2a$–$2d$ (see Fig. 4), which are characterized by mixing angles θ_{18} and θ_{20}:

$$|2a\rangle = \cos\theta_{18}|1(b)^3\Pi_0(v=17,J=18,e)\rangle - \sin\theta_{18}|2(A)^1\Sigma^+(v=18,J=18,e)\rangle \tag{17a}$$

$$|2b\rangle = \sin\theta_{18}|1(b)^3\Pi_0(v=17,J=18,e)\rangle + \cos\theta_{18}|2(A)^1\Sigma^+(v=18,J=18,e)\rangle \tag{17b}$$

$$|2c\rangle = \cos\theta_{20}|1(b)^3\Pi_0(v=17,J=20,e)\rangle - \sin\theta_{20}|2(A)^1\Sigma^+(v=18,J=20,e)\rangle \tag{17c}$$

$$|2d\rangle = \sin\theta_{20}|1(b)^3\Pi_0(v=17,J=20,e)\rangle + \cos\theta_{20}|2(A)^1\Sigma^+(v=18,J=20,e)\rangle. \tag{17d}$$

In these expressions, $\cos\theta_{19\pm 1}$ and $\sin\theta_{19\pm 1}$ are defined by equations that are analogous to Eqs. (9), but where we define $\Delta E^0 \equiv E_{A^1\Sigma^+(v=18,J=19\pm 1,e)} - E_{b^3\Pi_0(v=17,J=19\pm 1,e)} > 0$ since it was shown in Ref. [14] that the lower energy level in each pair ($2a$ and $2c$) is the predominantly triplet component of the $J=18$ and 20 mixed levels, respectively, and $H_{\text{SO}} = \langle A^1\Sigma^+(18,\ \ 19\pm 1)|H_{\text{SO}}|b^3\Pi_0(17,\ \ 19\pm 1)\rangle$. Again, $\cos\theta_{19\pm 1} > 0$ and $\sin\theta_{19\pm 1}$ carries the same sign as H_{SO}.

For excitation of the upper level $3i$ from any of these mixed intermediate levels $2j$ the rate equations yield

$$n_{3i} = \frac{B_{3i\leftarrow 2j} I_{\text{probe}} n_{2j}}{\Gamma_{3i}}. \tag{18}$$

However in this case, the Einstein B coefficient for absorption has contributions from singlet and triplet excitation channels. For example, for excitation of level $3a$ from level $2a$ we find

$$B_{3a\leftarrow 2a} \propto |-\cos\varphi\sin\theta_{18}\langle 3^1\Pi_1(6,19)|\hat{\varepsilon}\cdot\vec{\mu}\,|A^1\Sigma^+(18,18)\rangle - \sin\varphi\cos\theta_{18}\langle 3^3\Pi_0(32,19)|\hat{\varepsilon}\cdot\vec{\mu}\,|b^3\Pi_0(17,18)\rangle|^2, \tag{19}$$

where we must now add the amplitudes before squaring. Using the same analysis as before, the fluorescence signal associated with level $3a$ recorded in the green detection channel, can be written as

$$(I_{3a\leftarrow 2a})_{\text{green}} \propto \varepsilon_{3^3\Pi\rightarrow a^3\Sigma^+}\sin^2\varphi\frac{\Gamma_{3^3\Pi\rightarrow a^3\Sigma^+}}{\Gamma_{3a}} I_{\text{probe}} n_{2a} \times |\cos\varphi\sin\theta_{18}\langle 3^1\Pi_1(6,19)|\hat{\varepsilon}\cdot\vec{\mu}\,|A^1\Sigma^+(18,18)\rangle + \sin\varphi\cos\theta_{18}\langle 3^3\Pi_0(32,19)|\hat{\varepsilon}\cdot\vec{\mu}\,|b^3\Pi_0(17,18)\rangle|^2. \tag{20a}$$

Similarly we find

$$(I_{3b\leftarrow 2a})_{\text{green}} \propto \varepsilon_{3^3\Pi\rightarrow a^3\Sigma^+}\cos^2\varphi\frac{\Gamma_{3^3\Pi\rightarrow a^3\Sigma^+}}{\Gamma_{3b}} I_{\text{probe}} n_{2a} \times |-\sin\varphi\sin\theta_{18}\langle 3^1\Pi_1(6,19)|\hat{\varepsilon}\cdot\vec{\mu}\,|A^1\Sigma^+(18,18)\rangle + \cos\varphi\cos\theta_{18}\langle 3^3\Pi_0(32,19)|\hat{\varepsilon}\cdot\vec{\mu}\,|b^3\Pi_0(17,18)\rangle|^2. \tag{20b}$$

In these expressions, we see the origins of both constructive and destructive interference between the singlet and triplet excitation channels. The ratio of these fluorescence signals can be expressed as

$$\left(\frac{I_{3a\leftarrow 2a}}{I_{3b\leftarrow 2a}}\right)_{\text{green}} = \frac{\sin^2\varphi}{\cos^2\varphi}\frac{\Gamma_{3b}}{\Gamma_{3a}} \times \frac{|\cos\varphi\sin\theta_{18}\langle 3^1\Pi_1(6,19)|\hat{\varepsilon}\cdot\vec{\mu}\,|A^1\Sigma^+(18,18)\rangle + \sin\varphi\cos\theta_{18}\langle 3^3\Pi_0(32,19)|\hat{\varepsilon}\cdot\vec{\mu}\,|b^3\Pi_0(17,18)\rangle|^2}{|-\sin\varphi\sin\theta_{18}\langle 3^1\Pi_1(6,19)|\hat{\varepsilon}\cdot\vec{\mu}\,|A^1\Sigma^+(18,18)\rangle + \cos\varphi\cos\theta_{18}\langle 3^3\Pi_0(32,19)|\hat{\varepsilon}\cdot\vec{\mu}\,|b^3\Pi_0(17,18)\rangle|^2}. \quad (21)$$

Fig. 3b shows green fluorescence signals recorded when the mixed pair $3^3\Pi_0(v=32,J=19,e)\sim 3^1\Pi_1(v=6,J=19,e)$ (i.e. levels $3a$ and $3b$) was excited from the predominantly triplet component (level $2a$) of the intermediate level pair $1(b)^3\Pi_0(v=17,J=18)\sim 2(A)^1\Sigma^+(v=18,\ J=18)$ (R line excitation). Essentially complete destructive interference is observed in the $3a\leftarrow 2a$ excitation channel, implying that the numerator in Eq. (21) is much smaller than the denominator.

Fig. 3c shows green fluorescence signals recorded when the same mixed pair $3^3\Pi_0(v=32,J=19,\ e)\sim 3^1\Pi_1(v=6,\ J=19,\ e)$ was excited from the predominantly triplet component (level $2c$) of the intermediate level pair $1(b)^3\Pi_0(v=17,J=20)\sim 2(A)^1\Sigma^+(v=18,J=20)$ (P line excitation). Using the same arguments as before we can write the following expression for the fluorescence ratio

$$\left(\frac{I_{3a\leftarrow 2c}}{I_{3b\leftarrow 2c}}\right)_{\text{green}} = \frac{\sin^2\varphi}{\cos^2\varphi}\frac{\Gamma_{3b}}{\Gamma_{3a}} \times \frac{|\cos\varphi\sin\theta_{20}\langle 3^1\Pi_1(6,19)|\hat{\varepsilon}\cdot\vec{\mu}\,|A^1\Sigma^+(18,20)\rangle + \sin\varphi\cos\theta_{20}\langle 3^3\Pi_0(32,19)|\hat{\varepsilon}\cdot\vec{\mu}\,|b^3\Pi_0(17,20)\rangle|^2}{|-\sin\varphi\sin\theta_{20}\langle 3^1\Pi_1(6,19)|\hat{\varepsilon}\cdot\vec{\mu}\,|A^1\Sigma^+(18,20)\rangle + \cos\varphi\cos\theta_{20}\langle 3^3\Pi_0(32,19)|\hat{\varepsilon}\cdot\vec{\mu}\,|b^3\Pi_0(17,20)\rangle|^2}. \quad (22)$$

In this case, essentially complete destructive interference is observed in the $3b\leftarrow 2c$ excitation channel, implying that the denominator of Eq. (22) is much smaller than the numerator.

We note here that the sign of the interference is an observable quantity and therefore it cannot depend on the arbitrary phase of any basis function. The cross terms in Eqs. (21) and (22) involve the product $\sin\varphi\cos\varphi\sin\theta_{19\pm1}\cos\theta_{19\pm1}\langle 3^1\Pi_1(6,19)|\hat{\varepsilon}\cdot\vec{\mu}\,|A^1\Sigma^+(18,19\pm1)\rangle\langle b^3\Pi_0(17,19\pm1)|\hat{\varepsilon}\cdot\vec{\mu}\,|3^3\Pi_0(32,19)\rangle$. From Eqs. (9), it is easy to show that $\sin\varphi\cos\varphi = \frac{1}{2}H_{\text{SO}}[H_{\text{SO}}^2+(\Delta E^0/2)^2]^{-1/2}$, and thus is proportional to, and takes the sign of, the corresponding spin orbit matrix element $\langle 3^3\Pi_0(32,19)|H_{\text{SO}}|3^1\Pi_1(6,19)\rangle$. Similarly, $\sin\theta_{19\pm1}\cos\theta_{19\pm1} \propto \langle A^1\Sigma^+(18,19\pm1)|H_{\text{SO}}|b^3\Pi_0(17,19\pm1)\rangle$. Therefore, the sense of the interference effect is determined by the product of two transition moments and two perturbation matrix elements. Each electronic and vibrational wavefunction appears twice in this product; once as a bra and once as a ket. Thus the result is not affected by the arbitrary phase choice for the basis functions.

In the two cases discussed above, the upper levels have comparable singlet and triplet amplitudes, while the intermediate levels have quite different singlet and triplet amplitudes (both ~86% triplet according to Ref. [14]). But this is compensated by the much larger singlet channel dipole matrix element, so that almost complete cancellation can be observed. We also note that although $\theta_{18}\approx\theta_{20}$, the obvious sign difference between the numerator of Eq. (21) and the denominator of (22) (the two cases where almost complete cancellation is observed) can be attributed to the difference in the sign of the R and P line singlet dipole matrix elements (see below).

According to Ref. [52] (Section 6.3.2), in the space fixed coordinate system (XYZ) and with a linearly polarized probe laser (polarized along Z), we can write

$$\hat{\varepsilon}\cdot\vec{\mu} = \mu_Z = \frac{1}{2}\alpha_Z^+\mu^- + \frac{1}{2}\alpha_Z^-\mu^+ + \alpha_Z^z\mu_z, \quad (23)$$

where the $\alpha_I^j \equiv \hat{I}\cdot\hat{j}$ are direction cosine operator components linking unit vectors in the space fixed (XYZ) and body fixed (xyz) coordinate systems, $\alpha_Z^\pm \equiv \alpha_Z^x \pm i\alpha_Z^y$ and $\mu^\pm \equiv \mu_x \pm i\mu_y$. This expression allows us to factor dipole matrix elements into electronic-transition-specific, molecule-fixed, nonrotating molecule matrix elements of μ_j times rotating molecule matrix elements of α_Z^j. Writing the molecular wavefunctions as products $|\Omega JM\rangle|n\Lambda S\Sigma\rangle$, where n specifies the electronic state and vibrational level, S is the electronic spin, Σ and Λ are the projections of electron spin and electron orbital angular momenta onto the internuclear axis, $\Omega=\Lambda+\Sigma$, and M is the component of the nuclear rotation J along the laboratory fixed Z axis, it can be shown that for $\Delta\Omega=0$ transitions

$$\langle n'\Lambda S\Sigma|\langle\Omega J'M|\mu_Z|\Omega J''M\rangle|n''\Lambda S\Sigma\rangle = \mu_\parallel[n'\Lambda,n''\Lambda]\langle\Omega J'M|\alpha_Z^z|\Omega J''M\rangle, \quad (24a)$$

while for $\Delta\Omega=\pm1$ transitions

$$\langle n'(\Lambda\pm1)S\Sigma|\langle(\Omega\pm1)J'M|\mu_Z|\Omega J''M\rangle|n''\Lambda S\Sigma\rangle = \frac{1}{\sqrt{2}}\mu_\perp[n'(\Lambda\pm1),n''\Lambda]\langle(\Omega\pm1)J'M|\alpha_Z^{\mp}|\Omega J''M\rangle. \quad (24b)$$

In these expressions, $\mu_\parallel[n'\Lambda,n''\Lambda]\equiv\langle n'\Lambda|\mu_z|n''\Lambda\rangle$ and $\frac{1}{\sqrt{2}}\mu_\perp[n'(\Lambda\pm1),n''\Lambda]\equiv\langle n'(\Lambda\pm1)|\mu^{\pm}|n''\Lambda\rangle$. Using *e*/*f* symmetrized basis functions $\frac{1}{\sqrt{2}}\{|\Omega JM\rangle|n\Lambda S\Sigma\rangle\pm|-\Omega JM\rangle|n,-\Lambda,S,-\Sigma\rangle\}$, corresponding to the observed levels in the present case, one can show that the factor of $1/\sqrt{2}$ in Eq. (24b) does not appear for $\Sigma^+\rightarrow\Pi$ transitions [52]. Evaluating the matrix elements of α_Z^j with the help of Ref. [72] (Table 6, page 31), we find

$$\begin{aligned}\langle 3^3\Pi_0(32,J)|\mu_Z|b^3\Pi_0(17,J-1)\rangle &= \mu_\parallel[3^3\Pi(v=32),b^3\Pi(v=17)]\frac{1}{(J)}\\ &\times\left[\frac{(J+\Omega)(J-\Omega)(J+M)(J-M)}{(2J-1)(2J+1)}\right]^{1/2}\\ &= \mu_\parallel[3^3\Pi(v=32),b^3\Pi(v=17)]\left[\frac{(J+M)(J-M)}{(2J-1)(2J+1)}\right]^{1/2}\end{aligned} \quad (25a)$$

$$\begin{aligned}\langle 3^3\Pi_0(32,J)|\mu_Z|b^3\Pi_0(17,J+1)\rangle &= \mu_\parallel[3^3\Pi(v=32),b^3\Pi(v=17)]\frac{1}{(J+1)}\\ &\times\left[\frac{(J+\Omega+1)(J-\Omega+1)(J+M+1)(J-M+1)}{(2J+3)(2J+1)}\right]^{1/2}\\ &= \mu_\parallel[3^3\Pi(v=32),b^3\Pi(v=17)]\\ &\times\left[\frac{(J+M+1)(J-M+1)}{(2J+3)(2J+1)}\right]^{1/2}\end{aligned} \quad (25b)$$

$$\begin{aligned}\langle 3^1\Pi_1(6,J)|\mu_Z|A^1\Sigma^+(18,J-1)\rangle &= -\mu_\perp[3^1\Pi(v=6),A^1\Sigma^+(v=18)]\frac{1}{(J)}\\ &\times\left[\frac{(J+\Omega)(J+\Omega+1)(J+M)(J-M)}{(2J-1)(2J+1)}\right]^{1/2}\\ &= -\mu_\perp[3^1\Pi(v=6),A^1\Sigma^+(v=18)]\left[\frac{(J+1)}{J}\right]^{1/2}\\ &\times\left[\frac{(J+M)(J-M)}{(2J-1)(2J+1)}\right]^{1/2}\end{aligned} \quad (25c)$$

$$\begin{aligned}\langle 3^1\Pi_1(6,J)|\mu_Z|A^1\Sigma^+(18,J+1)\rangle &= \mu_\perp[3^1\Pi(v=6),A^1\Sigma^+(v=18)]\frac{1}{(J+1)}\\ &\times\left[\frac{(J-\Omega+1)(J-\Omega)(J+M+1)(J-M+1)}{(2J+3)(2J+1)}\right]^{1/2}\\ &= \mu_\perp[3^1\Pi(v=6),A^1\Sigma^+(v=18)]\left[\frac{J}{(J+1)}\right]^{1/2}\\ &\times\left[\frac{(J+M+1)(J-M+1)}{(2J+3)(2J+1)}\right]^{1/2}\end{aligned} \quad (25d)$$

where in the second step of each expression we have used the fact that $\Omega=0$ for the lower state of each transition. The critical minus sign appearing in Eq. (25c) but not Eq. (25d) is responsible for the reversal of the constructive and destructive interference for the two upper levels when they are excited using *R* vs. *P* line pumping. Quantum interference occurs for each value of *M* separately, and we can derive a relationship between the fluorescence ratios and the ratio of singlet and triplet channel electronic dipole matrix elements. Inserting (25a) and (25c) into Eq. (21) with $J=19$, and noting that the *M* dependent terms cancel, we find

$$\left(\frac{I_{3a\leftarrow2a}}{I_{3b\leftarrow2a}}\right)_{\text{green}} = \frac{\sin^2\varphi}{\cos^2\varphi}\frac{\Gamma_{3b}}{\Gamma_{3a}} \times\frac{\left|-\frac{\mu_\perp[3^1\Pi(v=6),A^1\Sigma^+(v=18)]}{\mu_\parallel[3^3\Pi(v=32),b^3\Pi(v=17)]}\left(\frac{20}{19}\right)^{1/2}+\tan\varphi\cot\theta_{18}\right|^2}{\left|\tan\varphi\frac{\mu_\perp[3^1\Pi(v=6),A^1\Sigma^+(v=18)]}{\mu_\parallel[3^3\Pi(v=32),b^3\Pi(v=17)]}\left(\frac{20}{19}\right)^{1/2}+\cot\theta_{18}\right|^2}. \quad (26a)$$

Similarly, inserting (25b) and (25d) into Eq. (22) we obtain

$$\left(\frac{I_{3a\leftarrow2c}}{I_{3b\leftarrow2c}}\right)_{\text{green}} = \frac{\sin^2\varphi}{\cos^2\varphi}\frac{\Gamma_{3b}}{\Gamma_{3a}} \times\frac{\left|\frac{\mu_\perp[3^1\Pi(v=6),A^1\Sigma^+(v=18)]}{\mu_\parallel[3^3\Pi(v=32),b^3\Pi(v=17)]}\left(\frac{19}{20}\right)^{1/2}+\tan\varphi\cot\theta_{20}\right|^2}{\left|-\tan\varphi\frac{\mu_\perp[3^1\Pi(v=6),A^1\Sigma^+(v=18)]}{\mu_\parallel[3^3\Pi(v=32),b^3\Pi(v=17)]}\left(\frac{19}{20}\right)^{1/2}+\cot\theta_{20}\right|^2}. \quad (26b)$$

When the upper levels 3*a* and 3*b* are excited from the predominantly singlet components (2*b* and 2*d*) of the mixed intermediate states, we again observe interference effects. But in these cases, only a partial cancellation is observed. Fig. 3d and e show the corresponding fluorescence scans. Using similar arguments to those above, we calculate the intensity ratios $(I_{3a\leftarrow2b}/I_{3b\leftarrow2b})_{\text{green}}$ and $(I_{3a\leftarrow2d}/I_{3b\leftarrow2d})_{\text{green}}$ associated with excitation from these predominantly singlet components of the intermediate window levels. We find

$$\begin{aligned}\left(\frac{I_{3a\leftarrow2b}}{I_{3b\leftarrow2b}}\right)_{\text{green}} &= \frac{\sin^2\varphi}{\cos^2\varphi}\frac{\Gamma_{3b}}{\Gamma_{3a}}\frac{|\cos\varphi\cos\theta_{18}\langle3^1\Pi_1(6,19)|\hat{\varepsilon}\cdot\vec{\mu}\,|A^1\Sigma^+(18,18)\rangle-\sin\varphi\sin\theta_{18}\langle3^3\Pi_0(32,19)|\hat{\varepsilon}\cdot\vec{\mu}\,|b^3\Pi_0(17,18)\rangle|^2}{|\sin\varphi\cos\theta_{18}\langle3^1\Pi_1(6,19)|\hat{\varepsilon}\cdot\vec{\mu}\,|A^1\Sigma^+(18,18)\rangle+\cos\varphi\sin\theta_{18}\langle3^3\Pi_0(32,19)|\hat{\varepsilon}\cdot\vec{\mu}\,|b^3\Pi_0(17,18)\rangle|^2}\\ &= \frac{\sin^2\varphi}{\cos^2\varphi}\frac{\Gamma_{3b}}{\Gamma_{3a}}\frac{\left|-\frac{\mu_\perp[3^1\Pi(v=6),A^1\Sigma^+(v=18)]}{\mu_\parallel[3^3\Pi(v=32),b^3\Pi(v=17)]}\left(\frac{20}{19}\right)^{1/2}-\tan\varphi\tan\theta_{18}\right|^2}{\left|-\tan\varphi\frac{\mu_\perp[3^1\Pi(v=6),A^1\Sigma^+(v=18)]}{\mu_\parallel[3^3\Pi(v=32),b^3\Pi(v=17)]}\left(\frac{20}{19}\right)^{1/2}+\tan\theta_{18}\right|^2}\end{aligned} \quad (27a)$$

and

$$\left(\frac{I_{3a\leftarrow 2d}}{I_{3b\leftarrow 2d}}\right)_{\text{green}} = \frac{\sin^2\varphi}{\cos^2\varphi}\frac{\Gamma_{3b}}{\Gamma_{3a}}\frac{|\cos\varphi\cos\theta_{20}\langle 3^1\Pi_1(6,19)|\hat{\varepsilon}\cdot\vec{\mu}\,|A^1\Sigma^+(18,20)\rangle - \sin\varphi\sin\theta_{20}\langle 3^3\Pi_0(32,19)|\hat{\varepsilon}\cdot\vec{\mu}\,|b^3\Pi_0(17,20)\rangle|^2}{|\sin\varphi\cos\theta_{20}\langle 3^1\Pi_1(6,19)|\hat{\varepsilon}\cdot\vec{\mu}\,|A^1\Sigma^+(18,20)\rangle + \cos\varphi\sin\theta_{20}\langle 3^3\Pi_0(32,19)|\hat{\varepsilon}\cdot\vec{\mu}\,|b^3\Pi_0(17,20)\rangle|^2}$$
$$= \frac{\sin^2\varphi}{\cos^2\varphi}\frac{\Gamma_{3b}}{\Gamma_{3a}}\frac{\left|\frac{\mu_\perp[3^1\Pi(v=6),A^1\Sigma^+(v=18)]}{\mu_\parallel[3^3\Pi(v=32),b^3\Pi(v=17)]}\left(\frac{19}{20}\right)^{1/2} - \tan\varphi\tan\theta_{20}\right|^2}{\left|\tan\varphi\frac{\mu_\perp[3^1\Pi(v=6),A^1\Sigma^+(v=18)]}{\mu_\parallel[3^3\Pi(v=32),b^3\Pi(v=17)]}\left(\frac{19}{20}\right)^{1/2} + \tan\theta_{20}\right|^2}. \quad (27b)$$

We note that for violet fluorescence (singlet channel) detection, the leading $\sin^2\varphi/\cos^2\varphi$ factor in Eqs. (26) and (27) is simply replaced by $\cos^2\varphi/\sin^2\varphi$.

Green and violet fluorescence signals were recorded following excitation of levels 3*a* and 3*b* from all five levels 2, 2*a*, 2*b*, 2*c*, and 2*d*. According to Eqs. (13), (26) and (27) and the analogous expressions for violet fluorescence detection, the I_{3a}/I_{3b} fluorescence ratios depend on the three mixing angles φ, θ_{18}, and θ_{20}, the ratio of decay rates Γ_{3b}/Γ_{3a}, and the ratio $\frac{\mu_\perp[3^1\Pi(v=6),A^1\Sigma^+(v=18)]}{\mu_\parallel[3^3\Pi(v=32),b^3\Pi(v=17)]}$. These five parameters were varied to give the best fit (in the least-squares sense) to the measured intensity ratios. In each case, it was assumed that the ratio of the weak fluorescence component to the strong component could be measured to within ~0.02.

Table 2
Measured and calculated fluorescence ratios

Intermediate state level	Detection channel	$(I_{3a\leftarrow 2i}/I_{3b\leftarrow 2i})$ measured	$(I_{3a\leftarrow 2i}/I_{3b\leftarrow 2i})$ calculated
2	Green	1.06 ± 0.02	1.08 ± 0.02
2	Violet	2.86 ± 0.16	2.94 ± 0.12
2*a*	Green	0.016 ± 0.02	0.005 ± 0.005
2*a*	Violet	0.033 ± 0.02	0.013 ± 0.014
2*b*	Green	1.69 ± 0.06	1.66 ± 0.08
2*b*	Violet	4.81 ± 0.46	4.54 ± 0.28
2*c*	Green	24.0 ± 11.5	19.4 ± 6.5
2*c*	Violet	73.1 ± 106.8	53.0 ± 17.4
2*d*	Green	0.58 ± 0.02	0.58 ± 0.02
2*d*	Violet	1.59 ± 0.05	1.58 ± 0.08

In each case, the uncertainties in the measured ratios (when defined as the weaker component divided by the stronger component) are taken to be ~0.02. Calculated values are obtained using Eqs. (13), (26) and (27) and the analogous expressions for violet fluorescence detection, with the best fit parameters of Table 3.

Table 2 gives a comparison between the best fit calculated intensity ratios and the measured ratios. Table 3 gives the best fit parameters. Error bars were determined using techniques outlined in chapter 8 of Bevington's text [74].

5. Conclusions

In conclusion, we have studied the mutually perturbing $3^3\Pi_{\Omega=0,1,2}(v=32,J,\ e/f)$ and $3^1\Pi_{\Omega=1}(v=6,J,\ e/f)$ levels of the NaK molecule using the OODR technique. A deperturbation analysis has allowed us to determine the $3^3\Pi_{\Omega=0,1,2}(v=32)$ molecular constants, including the $3^3\Pi$ state spin–orbit constant $A_{v=32}=3.179\ \text{cm}^{-1}$. The latter is consistent with values reported in Ref. [15].

The $3^3\Pi_{\Omega=0}(v=32,J=19)\sim 3^1\Pi_{\Omega=1}(v=6,J=19)$ f symmetry pair is almost a perfect 50–50 singlet/triplet mixture. In fact, when these levels are populated from the $2(A)^1\Sigma^+(v=16,J=19)$ state and fluorescence is monitored in the green and violet detection channels, we can write an expression analogous to Eq. (15) that provides a direct determination of the mixing angle for this f symmetry pair:

$$\tan\varphi_f = \left[\frac{\left(I_{3a(f)\leftarrow A^1\Sigma^+(v=16,J=19)}/I_{3b(f)\leftarrow A^1\Sigma^+(v=16,J=19)}\right)_{\text{green}}}{\left(I_{3a(f)\leftarrow A^1\Sigma^+(v=16,J=19)}/I_{3b(f)\leftarrow A^1\Sigma^+(v=16,J=19)}\right)_{\text{violet}}}\right]^{1/4}. \quad (28)$$

Here $I_{3i(f)\leftarrow A^1\Sigma^+(v=16,J=19)}$ is the fluorescence signal recorded following excitation of the f symmetry analog of level 3*i*, and φ_f is the mixing angle. Our measurements show that $\left(I_{3a(f)\leftarrow A^1\Sigma^+(v=16,J=19)}/I_{3b(f)\leftarrow A^1\Sigma^+(v=16,J=19)}\right)_{\text{green}}\approx 0.94$ and $\left(I_{3a(f)\leftarrow A^1\Sigma^+(v=16,J=19)}/I_{3b(f)\leftarrow A^1\Sigma^+(v=16,J=19)}\right)_{\text{violet}}\approx 0.88$ (see

Table 3
Best fit parameters used to calculate the fluorescence ratios given in Table 2

Parameter	Interpretation	Best fit value	Other values
φ	Mixing angle for levels $\|3a\rangle$ and $\|3b\rangle$	(37.87 ± 0.24)°	
θ_{18}	Mixing angle for levels $\|2a\rangle$ and $\|2b\rangle$	(14.5 ± 1.3)°	21.6° Ref. [14][b]
θ_{20}	Mixing angle for levels $\|2c\rangle$ and $\|2d\rangle$	(20.5 ± 0.8)°	22.2° Ref. [14][b]
Γ_{3b}/Γ_{3a}	Ratio of decay rates of two upper levels	1.076 ± 0.022	
$(\Gamma_{3^3\Pi_0(32,19,e)}/\Gamma_{3^1\Pi_1(6,19,e)})$[a]	Ratio of $3^3\Pi$ and $3^1\Pi$ decay rates	1.35 ± 0.13	
$\frac{\mu_\perp[3^1\Pi(v=6),A^1\Sigma^+(v=18)]}{\mu_\parallel[3^3\Pi(v=32),b^3\Pi(v=17)]}$	Ratio of electronic-transition-specific nonrotating molecule dipole matrix elements	2.46 ± 0.10	

When possible, the parameter values are compared to those from other references. Uncertainties for the fitted parameters are 1σ.

[a] From Eq. (16).

[b] The phase convention adopted here is different from that used in Ref. [14]. Values from Ref. [14] reported here correspond to the phase convention of the present work.

Figs. 1b and d, respectively), indicating that $\varphi_f \approx 45.5°$. Therefore, from this analysis we find that the *f* symmetry pair is a 50.9–49.1 mixture, which is certainly consistent with our 50–50 hypothesis. This *f* symmetry pair also allows us to determine an accurate value for the $3^3\Pi_{\Omega=1}(v=32) \sim 3^1\Pi_{\Omega=1}(v=6)$ spin–orbit interaction constant. [We note that the small difference between the 50.9–49.1 mixing ratio determined here and the 50–50 mixing used to determine $|\xi|$ in Section 3, does not affect the value of $|\xi|$ at the level of accuracy with which it is reported in Eq. (5).]

In addition, we observed quantum interference in the $3^3\Pi_{\Omega=0}(v=32, J=19) \sim 3^1\Pi_{\Omega=1}(v=6, J=19)$ *e* symmetry levels when they are populated from mixed singlet/triplet intermediate state levels. From the measured fluorescence ratios we were able to determine the mixing angle of the upper levels $3^3\Pi_{\Omega=0}(v=32, J=19, e) \sim 3^1\Pi_{\Omega=1}(v=6, J=19, e)$ and of the intermediate levels $1(b)^3\Pi_{\Omega=0}(v=17,\ J=18) \sim 2(A)^1\Sigma^+(v=18, J=18)$ and $1(b)^3\Pi_{\Omega=0}(v=17,\ J=20) \sim 2(A)^1\Sigma^+(v=18, J=20)$. We obtained $\varphi = (37.9 \pm 0.2)°$ for the $3^3\Pi_{\Omega=0}(v=32, J=19, e) \sim 3^1\Pi_{\Omega=1}(v=6, J=19, e)$ pair, indicating that this is a 38–62 singlet/triplet mixture. The values for the intermediate state mixing angles determined here, $\theta_{18} = (14.5 \pm 1.3)°$ and $\theta_{20} = (20.5 \pm 0.8)°$ are in fairly good agreement with the values $\theta_{18} \approx 21.6°$ and $\theta_{20} \approx 22.2°$ determined by Burns et al. [14] from the measured hyperfine splittings. (We note that the phase convention adopted here is different from that used in Ref. [14]. Values from Ref. [14] reported here correspond to the phase convention of the present work.) Thus Burns' analysis found that the $J = 18$ and 20 levels each form an 86–14 mixture while the present analysis indicates that the $J = 18$ pair is a 94–6 mixture and the $J = 20$ pair is an 88–12 mixture.

Finally, we have determined the ratio of decay rates for the $3^1\Pi_{\Omega=1}(v=6, J=19, e)$ and $3^3\Pi_{\Omega=0}(v=32, J=19, e)$ levels and the ratio of the singlet and triplet electronic transition dipole matrix elements. We found the decay rates to be in a ratio $\Gamma_{3^3\Pi_0(32,19,e)}/\Gamma_{3^1\Pi_1(6,19,e)} = (1.35 \pm 0.13)$, and the ratio of the transition matrix elements is $\frac{\mu_\perp[3^1\Pi(v=6),A^1\Sigma^+(v=18)]}{\mu_\parallel[3^3\Pi(v=32),b^3\Pi(v=17)]} \approx (2.46 \pm 0.10)$. As a comparison with the latter, we calculated the dipole matrix elements using the theoretical NaK potentials and transition dipole moments of Magnier et al. [75] in Le Roy's program LEVEL [71]. From these results, we determined a theoretical value of $\frac{\mu_\perp[3^1\Pi(v=6),A^1\Sigma^+(v=18)]}{\mu_\parallel[3^3\Pi(v=32),b^3\Pi(v=17)]} \approx 4.23$. However, the calculated ratio is extremely sensitive to the potentials used in the calculation. Using the experimental potentials of Refs. [15], [11], [76] and [77] with the theoretical transition dipole moments of Magnier et al., we calculate $\frac{\mu_\perp[3^1\Pi(v=6),A^1\Sigma^+(v=18)]}{\mu_\parallel[3^3\Pi(v=32),b^3\Pi(v=17)]} \approx 1.85$.

Acknowledgments

This work was supported by the National Science Foundation Grant No. PHY-0244767. S.E. was supported by the NSF REU site grant in the Department of Physics at Lehigh University and by a Goldwater Scholarship. We are grateful to Profs. Robert W. Field, Peet Hickman and Laurie Morgus for useful discussions.

Appendix A. Supplementary data

Supplementary data associated with this article are available on ScienceDirect (www.sciencedirect.com) and as part of the Ohio State University Molecular Spectroscopy Archives (http://msa.lib.ohio-state.edu/jmsa_hp.htm).

References

[1] D. DeMille, Phys. Rev. Lett. 88 (2002) 067901, 4 pages.
[2] T. Bergeman, A.J. Kerman, J. Sage, S. Sainis, D. DeMille, Eur. Phys. J. D 31 (2004) 179–188.
[3] H. Wang, W.C. Stwalley, J. Chem. Phys. 108 (1998) 5767–5771.
[4] S. Azizi, M. Aymar, O. Dulieu, Eur. Phys. J. D 31 (2004) 195–203.
[5] C. Haimberger, J. Kleinert, M. Bhattacharya, N.P. Bigelow, Phys. Rev. A 70 (2004) 021402(R), 4 pages.
[6] A.J. Kerman, J.M. Sage, S. Sainis, T. Bergeman, D. DeMille, Phys. Rev. Lett. 92 (2004) 033004, 4 pages.
[7] A.J. Kerman, J.M. Sage, S. Sainis, T. Bergeman, D. DeMille, Phys. Rev. Lett. 92 (2004) 153001, 4 pages.
[8] M. Masters, J. Huennekens, W.T. Luh, Li Li, A.M. Lyyra, K. Sando, V. Zafiropulos, W.C. Stwalley, J. Chem. Phys. 92 (1990) 5801–5813.
[9] H. Sun, J. Huennekens, J. Chem. Phys. 97 (1992) 4714–4722.
[10] Z.J. Jabbour, J. Huennekens, J. Chem. Phys. 107 (1997) 1094–1105.
[11] E. Laub, I. Mazsa, S.C. Webb, J. LaCivita, I. Prodan, Z.J. Jabbour, R.K. Namiotka, J. Huennekens, J. Mol. Spectrosc. 193 (1999) 376–388, *erratum* 221 (2003) 142–144.
[12] J. Huennekens, I. Prodan, A. Marks, L. Sibbach, E. Galle, T. Morgus, Li Li, J. Chem. Phys. 113 (2000) 7384–7397.
[13] P. Burns, L. Sibbach-Morgus, A.D. Wilkins, F. Halpern, L. Clarke, R.D. Miles, Li Li, A.P. Hickman, J. Huennekens, J. Chem. Phys. 119 (2003) 4743–4754.
[14] P. Burns, A.D. Wilkins, A.P. Hickman, J. Huennekens, J. Chem. Phys. 122 (2005) 074306, 8 pages.
[15] L. Morgus, P. Burns, R.D. Miles, A.D. Wilkins, U. Ogba, A.P. Hickman, J. Huennekens, J. Chem. Phys. 122 (2005) 144313, 10 pages.
[16] A.D. Wilkins, L. Morgus, J. Hernandez-Guzman, J. Huennekens, A.P. Hickman, J. Chem. Phys. 123 (2005) 124306, 12 pages.
[17] R.D. Miles, L. Morgus, D.O. Kashinski, J. Huennekens, A.P. Hickman, J. Chem. Phys. 125 (2006) 154304, 11 pages.
[18] Li Li, R.W. Field, J. Phys. Chem. 87 (1983) 3020–3022.
[19] X. Xie, R.W. Field, J. Mol. Spectrosc. 117 (1986) 228–244.
[20] Li Li, R.W. Field, J. Mol. Spectrosc. 123 (1987) 237–246.
[21] H. Katô, M. Otani, M. Baba, J. Chem. Phys. 91 (1989) 5124–5125.
[22] Li Li, Q. Zhu, R.W. Field, Mol. Phys. 66 (1989) 685–694.
[23] P. Kowalczyk, J. Chem. Phys. 91 (1989) 2779–2789.
[24] Li Li, A.M. Lyyra, W.T. Luh, W.C. Stwalley, J. Chem. Phys. 93 (1990) 8452–8463.
[25] H. Katô, M. Sakano, N. Yoshie, M. Baba, K. Ishikawa, J. Chem. Phys. 93 (1990) 2228–2237.
[26] T.-J. Whang, A.M. Lyyra, W.C. Stwalley, Li Li, J. Mol. Spectrosc. 149 (1991) 505–511.
[27] Li Li, T. An, T.-J. Whang, A.M. Lyyra, W.C. Stwalley, R.W. Field, R.A. Bernheim, J. Chem. Phys. 96 (1992) 3342–3343.
[28] K. Ishikawa, T. Kumauchi, M. Baba, H. Katô, J. Chem. Phys. 96 (1992) 6423–6432.
[29] Y.-C. Wang, K. Matsubara, H. Katô, J. Chem. Phys. 97 (1992) 811–817.
[30] A. Yiannopoulou, B. Ji, Li Li, M. Li, K. Urbanski, A.M. Lyyra, W.C. Stwalley, G.-H. Jeung, J. Chem. Phys. 101 (1994) 3581–3587.

[31] B. Ji, C.-C. Tsai, Li Li, T.-J. Whang, A.M. Lyyra, H. Wang, J.T. Bahns, W.C. Stwalley, R.J. Le Roy, J. Chem. Phys. 103 (1995) 7240–7254.
[32] J.T. Kim, H. Wang, C.C. Tsai, J.T. Bahns, W.C. Stwalley, G. Jong, A.M. Lyyra, J. Chem. Phys. 102 (1995) 6646–6652, erratum 103 (1995) 9891.
[33] Li Li, A. Yiannopoulou, K. Urbanski, A.M. Lyyra, B. Ji, W.C. Stwalley, T. An, J. Chem. Phys. 105 (1996) 6192–6199, erratum 106 (1997) 8626.
[34] Y. Liu, J. Li, H. Gao, D. Chen, Li Li, R.W. Field, A.M. Lyyra, J. Chem. Phys. 108 (1998) 2269–2276.
[35] Li Li, A.M. Lyyra, Spectrochim. Acta Part A 55 (1999) 2147–2178.
[36] X. Dai, J.O. Clevenger, Y. Liu, M. Song, J. Shang, D. Chen, R.W. Field, Li Li, J. Mol. Spectrosc. 200 (2000) 120–122.
[37] Y. Liu, B. Ji, A.S.-C. Cheung, W.C. Stwalley, R.W. Field, A.M. Lyyra, Li Li, J. Chem. Phys. 115 (2001) 3647–3656.
[38] Li Li, X. Dai, Y. Liu, J.O. Clevenger, R.W. Field, G.-H. Jeung, N. Geum, A.M. Lyyra, J. Mol. Spectrosc. 205 (2001) 139–145.
[39] P. Yi, M. Song, Y. Liu, A.M. Lyyra, Li Li, Chem. Phys. Lett. 349 (2001) 426–430.
[40] G. Lazarov, A.M. Lyyra, Li Li, J. Mol. Spectrosc. 205 (2001) 73–80.
[41] J. Magnes, E. Ahmed, C. Goldberg, A.M. Lyyra, S. Magnier, M. Aubert-Frécon, Y. Liu, Li Li, J. Mol. Spectrosc. 221 (2003) 72–79.
[42] Y. Liu, Li Li, G. Lazarov, A. Lazoudis, A.M. Lyyra, R.W. Field, J. Chem. Phys. 121 (2004) 5821–5827.
[43] P. Yi, X. Dai, J. Li, Y. Liu, Li Li, V.B. Sovkov, V.S. Ivanov, J. Mol. Spectrosc. 225 (2004) 33–38.
[44] Y. Chu, F. Xie, D. Li, Li Li, V.B. Sovkov, V.S. Ivanov, A.M. Lyyra, J. Chem. Phys. 122 (2005) 074302, 8 pages.
[45] E. Ahmed, A.M. Lyyra, Li Li, V.S. Ivanov, V.B. Sovkov, S. Magnier, J. Mol. Spectros. 229 (2005) 122–130.
[46] P. Qi, G. Lazarov, A.M. Lyyra, Y. Liu, C. Cui, Li Li, G.-H. Jeung, J. Chem. Phys. 124 (2006) 184304, 10 pages.
[47] C. Jungen, Can. J. Phys. 44 (1966) 3197–3216.
[48] G. Gouedard, J.C. Lehmann, J. Phys. B 9 (1976) 2113–2121.
[49] R.A. Gottscho, J.B. Koffend, R.W. Field, J.R. Lombardi, J. Chem. Phys. 68 (1978) 4110–4122.
[50] D. Stahel, M. Leoni, K. Dressler, J. Chem. Phys. 79 (1983) 2541–2558.
[51] C.W. Walter, P.C. Cosby, H. Helm, J. Chem. Phys. 112 (2000) 4621–4633.
[52] H. Lefebvre-Brion, R.W. Field, The Spectra and Dynamics of Diatomic Molecules, Elsevier, Amsterdam, 2004.
[53] A. Shnitman, I. Sofer, I. Golub, A. Yogev, M. Shapiro, Z. Chen, P. Brumer, Phys. Rev. Lett. 76 (1996) 2886–2889.
[54] T. Frohnmeyer, T. Baumert, Appl. Phys. B 71 (2000) 259–266.
[55] V.S. Batista, P. Brumer, J. Chem. Phys. 114 (2001) 10321–10331.
[56] B. Li, G. Turinici, V. Ramakrishna, H. Rabitz, J. Phys. Chem. B 106 (2002) 8125–8131.
[57] J.B. Ballard, H.U. Stauffer, E. Mirowski, S.R. Leone, Phys. Rev. A 66 (2002) 043402, 7 pages.
[58] M. Shapiro, P. Brumer, Rep. Prog. Phys. 66 (2003) 859–942.
[59] D. Goswami, Phys. Rep. 374 (2003) 385–481.
[60] M. Wollenhaupt, A. Assion, O. Bazhan, C. Horn, D. Liese, C. Sarpe-Tudoran, M. Winter, T. Baumert, Phys. Rev. A 68 (2003) 015401(R), 4 pages.
[61] B.H. Hosseini, H.R. Sadeghpour, N. Balakrishnan, Phys. Rev. A 71 (2005) 023402, 7 pages.
[62] A.K. Popov, S.A. Myslivets, T.F. George, Phys. Rev. A 71 (2005) 043811, 13 pages.
[63] R. Dumke, J.D. Weinstein, M. Johanning, K.M. Jones, P.D. Lett, Phys. Rev. A 72 (2005) 041801(R), 4 pages.
[64] K. Ohmori, H. Katsuki, H. Chiba, M. Honda, Y. Hagihara, K. Fujiwara, Y. Sato, K. Ueda, Phys. Rev. Lett. 96 (2006) 093002, 4 pages.
[65] S. Gerstenkorn, P. Luc, Atlas du Spectre D′Absorption de la Molécule D′Iode, Centre National de la Recherche Scientifique, Paris, 1978.
[66] A. Pashov, I. Jackowska, W. Jastrzębski, P. Kowalczyk, Phys. Rev. A 58 (1998) 1048–1054.
[67] Supplementary materials for this article include one table that can be retrieved from Science Direct.
[68] R.A. Gottscho, J.B. Koffend, R.W. Field, J. Mol. Spectrosc. 82 (1980) 310–338.
[69] A.J. Ross, C. Effantin, J. d'Incan, R.F. Barrow, Mol. Phys. 56 (1985) 903.
[70] I. Russier-Antoine, A.J. Ross, M. Aubert-Frécon, F. Martin, P. Crozet, J. Phys. B 33 (2000) 2753–2762.
[71] R.J. Le Roy, Level 7.5: A Computer Program for Solving the Radial Schrödinger Equation for Bound and Quasibound Levels, Chemical Physics Research Report No. CP-655 (University of Waterloo, 2002) (can be downloaded from the website http://leroy.uwaterloo.ca/programs/).
[72] J.T. Hougen, US Government Printing Office, National Bureau of Standards Monograph 115, Washington, DC, 1970.
[73] E.E. Whiting, R.W. Nicholls, Astrophys. J. Suppl. 27 (1974) 1–19.
[74] P.R. Bevington, Data Reduction and Error Analysis for the Physical Sciences, second ed., McGraw-Hill, New York, 1992.
[75] S. Magnier, M. Aubert-Frécon, Ph. Millié, J. Mol. Spectrosc. 200 (2000) 96–103.
[76] A.J. Ross, C. Effantin, J. d'Incan, R.F. Barrow, J. Phys. B 19 (1986) 1449–1456.
[77] A.J. Ross, R.M. Clements, R.F. Barrow, J. Mol. Spectrosc. 127 (1988) 546–548.